JAAS

CRITICAL REVIEW

View Article Online
View Journal | View Issue

Cite this: J. Anal. At. Spectrom., 2018, 33, 1600

U–Th–Pb geochronology and simultaneous analysis of multiple isotope systems in geological samples by LA-MC-ICP-MS

Lie-Wen Xie, *[ab] Noreen J. Evans, [c] Yue-Heng Yang, [ab] Chao Huang[ab] and Jin-Hui Yang[ab]

Laser ablation single/multiple collector inductively coupled plasma mass spectrometry (LA-SC/MC-ICP-MS) has become one of the most widely used *in situ* micro-analytical tools for the determination of isotopic ratios and trace element signatures in solid geological materials. The advantages include high spatial resolution, high sample throughput, good precision and accuracy, and limited sample preparation. For the application of these techniques in U–Th–Pb geochronology, the main challenges involve ion counter drift, matrix differences between reference materials and samples, laser-induced downhole elemental fractionation and common lead corrections. Given the requirement to achieve the maximum amount of geochemical information within the limited analytical domain of complexly zoned or small samples, simultaneous analysis of multiple isotopic systems and/or trace elements using laser ablation split stream (LASS) techniques is now widely applied. This article summarizes recent advances in LA-SC/MC-ICP-MS U–Th–Pb geochronology and LASS techniques. We review recent efforts to improve spatial resolution, calibrate ion counter drift, and correct for common lead contamination, elemental fractionation and matrix mismatching. A summary of the range of minerals utilized for LA-MC-ICP-MS geochronology and LASS is provided, along with a discussion of potential directions for future research.

Received 22nd May 2018
Accepted 16th August 2018

DOI: 10.1039/c8ja00157j

rsc.li/jaas

1. Introduction

Accurate U–Th–Pb geochronology of accessory minerals (*e.g.*, zircon, baddeleyite, monazite, apatite, rutile, titanite, allanite, xenotime, uraninite, perovskite, loparite, bastnaesite, eudialyite, columbite–tantalite, andradite, schorlomite and others) is critical for deciphering geological processes. The most commonly used techniques are isotope dilution thermal ionization mass spectrometry (ID-TIMS), secondary ion mass spectrometry (SIMS) and laser ablation single/multiple collector inductively coupled plasma mass spectrometry (LA-SC/MC-ICP-MS). Walder *et al.* (1993)[1] successfully introduced a method for measuring the Pb isotope ratios of solid samples, showing its potential to yield very high-precision isotopic ratio measurements for natural materials with high spatial resolution. Laser probe methods provide several advantages over high precision ID-TIMS including the ability to directly and rapidly measure small volumes of material with limited sample preparation, and to provide ages at a high spatial resolution, with accuracy to within 1% of those obtained using ID-TIMS (*e.g.*, ref. 2), although it is also important to consider error propagation when inter-method comparisons are made.[3] In addition, compared with the relatively time-consuming SIMS approach, laser methods offer higher ionization efficiency and analytical throughput (particularly if data acquisition on the MS is triggered from an automated laser sequence, accommodating hundreds of ablations in a single day), with lower polyatomic interference (particularly in the case of the newly introduced tandem MS/collision cell MS systems; *e.g.* Agilent 8900-QQQ, Thermo Fisher TQ series; Nu Plasma Sapphire) and matrix effects.

Measurement of isotopic compositions by LA-MC-ICP-MS (multi-collector) offers significant advantages over LA-SC-ICP-MS (single collector) methods. Multi-collectors simultaneously measure all isotopic signals over flat-topped peaks so that (1) the detection efficiency is significantly improved and relatively high spatial resolution is obtained,[4,5] and (2) the effects of spectral skew and flicker noise from the plasma source or ablated particles are removed or significantly reduced, resulting in improved counting statistics and lower internal and external uncertainties in isotopic ratios.[2,6,7] As a consequence, LA-MC-ICP-MS techniques have rapidly developed and are now widely used for geochronology and isotopic geochemistry (*e.g.*, measuring Sr, Nd, Hf and U–Th–Pb isotopic ratios), with high

[a]State Key Laboratory of Lithospheric Evolution, Institute of Geology and Geophysics, Chinese Academy of Sciences, P. O. Box 9825, Beijing 100029, P. R. China. E-mail: xieliewen@mail.iggcas.ac.cn; Fax: +86-010-62010846; Tel: +86-010-82998599
[b]Institutions of Earth Science, Chinese Academy of Sciences, P. O. Box 9825, Beijing 100029, P. R. China
[c]School of Earth and Planetary Science, John de Laeter Centre, Curtin University, WA, Australia

precision and accuracy and at high spatial resolution (*e.g.*, ref. 1 and 8–11).

For studies on complexly zoned minerals, small grains (<10 microns) and detrital/inherited minerals, researchers must obtain the maximum amount of geochemical information (geochronology, isotope composition and trace element concentration) on a single ablated volume. The coupling of laser systems and more than one MS system where the carrier gas flow (and, therefore, the ablated product) is split between the mass spectrometers has been termed laser ablation split stream (LASS) analysis.[12,13] Simultaneous measurement of isotopic signatures (*e.g.* U–Th–Pb and Lu–Hf, U–Th–Pb and Sm–Nd, and Sm–Nd and Lu–Hf) on a MC-ICP-MS and trace elements (or U–Th–Pb) on a SC-ICP-MS (or another MC-ICP-MS/high resolution ICP-MS) means that several datasets can be obtained on a single ablation volume, preserving provenance information and the spatial relationship between key chronological and geochemical tracer records (*e.g.*, ref. 4 and 12–17).

In this article we provide an overview of LA-MC-ICP-MS dating techniques with ion counter (IC) calibrations, and corrections for common lead, mass fractionation and matrix matching issues. Recent improvements in ultra-high spatial resolution U–Th–Pb dating is reviewed, as is the current state of LASS analysis in various mineral phases. Finally, we present our perspective on future developments that might further resolve the challenges associated with these techniques.

2. Background

The significant increase in the availability of inductively coupled plasma mass spectrometers with multiple Faraday collectors (MFCs) and/or multiple ion counters (MICs) has greatly improved research on stable and radiogenic isotopic systems in the past two decades. Coupled with laser ablation (LA) systems (including nanosecond or femtosecond lasers), *in situ* high spatial resolution isotope analysis of solid geological samples has become relatively routine. The MFC systems can provide a wider dynamic linear range of over five to six orders of magnitude and a more stable performance, compared with the MIC systems, which utilize the standard–sample bracketing technique (SSB).[18] Laser ablation or solution sampling MFC-ICP-MS systems yield Sr, Nd and Hf isotope compositions with high precision, using an internal isotope pair to correct for mass fractionation.[9,19,20] However, a Faraday cup is about 100 times less sensitive than a secondary electron multiplier (SEM).[21] The signal to noise ratio of Faraday collectors with the default 10^{11} ohm amplifier is too low to obtain high precision data when the signal intensities are low,[22,23] and the application of LA-MFC-ICP-MS techniques to U–Th–Pb dating is limited to either very old minerals or minerals with a high U content and high radiogenic Pb complement (*e.g.*, ref. 2, 22, 24 and 25).

To improve the precision of measurements obtained using small ion beams on MFC systems, amplifiers equipped with 10^{12} and 10^{13} ohm resistors in the feedback loop were developed, increasing the gain by a factor of 10 and 100 times and improving the theoretical signal to noise ratio by a factor of 3 and 10, respectively, compared to the default 10^{11} ohm resistors.[23] For example, Kimura *et al.* (2015)[26] used a 193 nm excimer laser and 200/266 nm femtosecond laser coupled with an enhanced sensitivity MFC-ICP-MS (Neptune) using 10^{12} ohm amplifiers to determine the U–Pb ages of reference zircon and monazite crystals with an internal precision of 1–2% from a crater of dimensions 50 μm × 10 μm (diameter × depth) at a repetition rate of 2 Hz for 30 s.

In contrast, the MIC system provides a powerful ability to measure small ion signals, which are the norm for high spatial resolution U–Th–Pb dating.[23] The precision of the measured $^{206}Pb/^{207}Pb$ ratio on two ion counters is remarkably superior to that produced by an ion counter in conjunction with a Faraday cup (with the 10^{11} ohm amplifier) when the measured signals are less than 12.5 mV (Fig. 1).[5] Many MC-ICP-MS instruments can be equipped with a series of MFC and MIC detectors with the primary analytical application dictating the ideal detector configuration. In U–Th–Pb dating, one detector configuration places the Hg isotopes and most/all of the Pb isotopes on ion counters and the other isotopes (including ^{232}Th, ^{235}U and ^{238}U) on Faraday cups, such as in the U–Th–Pb dating of zircon, monazite, and titanite by Simonetti *et al.* (2006).[27] An alternate approach places all measured isotopes on ion counters, such as U–Pb dating of zircon by Hattori *et al.* (2017)[7] and Xie *et al.* (2017).[5] The precision of zircon U–Pb dating with MIC systems is about 1% (2 s), which is comparable to that achieved by SIMS at high ion intensities.[28,29] The stability of ion counters, however, is worse than that of Faraday cups. Some aspects of MIC systems, such as non-linear behavior, drift in counting efficiency depending on the count rate, and the difficulty in determining the IC dead time, can limit their precision.[7,30]

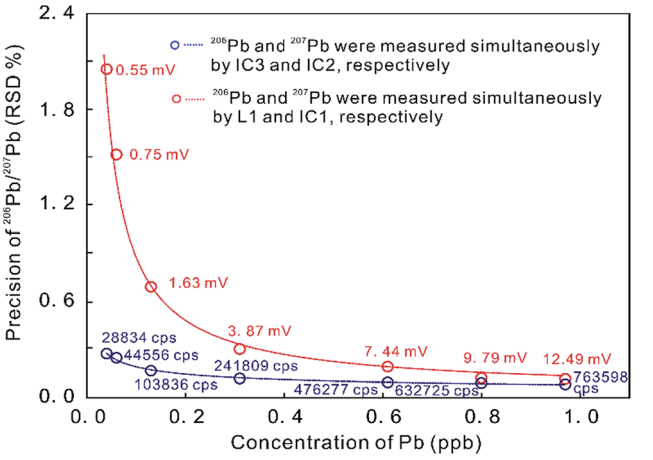

Fig. 1 Precision of Pb ratio determination at a range of Pb concentrations as measured on ion counters and on a combination of ion counters and Faraday cups (with a 10^{11} ohm amplifier) on a Neptune Plus MC-ICP-MS. Red data indicate ^{206}Pb signal intensities on L1 in millivolt [mV] and blue data indicate ^{206}Pb signal intensities on IC3 in counts per second [cps]. Better internal $^{206}Pb/^{207}Pb$ precision was obtained in MIC mode, compared to using a combination of ion counters and Faraday cups (from ref. 5).

3. U–Th–Pb geochronology

3.1 Ion counter corrections

The secondary electron multiplier (SEM) is used extensively as an ion detector in mass spectrometers. A typical discrete dynode electron multiplier has 12 to 24 dynodes, and can amplify a small ion current by a factor of 10^4–10^8.[31] This ability makes it valuable for *in situ* laser ablation analysis of geological samples where a highly sensitive detection method is required. Applications using SEMs in ion counting mode, however, suffer from variability in detection efficiency, which is associated with time and ion beam size.[7,30,32] In order to obtain high accuracy and precision chronological data using LA-MC-ICP-MS systems with ion counters, it is necessary to characterize each detector in detail so that corrections can be applied (*e.g.* cross-calibration of the relative yield between ion counters and/or Faraday cups, dead time and non-linearity).

When the operating voltage of a SEM is at its plateau, almost all incident ions are detected. A beam with an ion count rate of 6.25×10^7 cps (counts per second) measured on a SEM should theoretically produce a signal intensity of 1 V on a Faraday cup with a 10^{11} ohm resistor. In fact, the count rate responses between Faraday cups and SEMs are different, and these two detection systems have to be experimentally cross-calibrated to obtain the FC-SEM yield.[33] Previous studies have described different methods for determining FC-SEM yield.[28,33,34]

Detector dead time is the time during which the ion counting system is unable to count incoming ions after the impact of a previous ion. This parameter is a feature of both the detector itself and the ion counting electronics, which depend on the pulse amplifiers.[30] Dead time is corrected by applying the equation $I_t = I_0/(1 - I_0\tau)$, where I_t is the count rate corrected for dead time losses, I_0 is the count rate obtained with no dead time correction applied (*i.e.*, dead time ~0 ns) and τ is the apparent dead time of the detection system.[31] Several methods have been developed to determine the dead time (*e.g.*, ref. 35–38). Nelms *et al.* (2001)[32] evaluated four methods of dead time calculation on two quadrupole SC-ICP-MS instruments and found that the most suitable method was the one based on studies of the $^{204}Pb/^{208}Pb$ isotope ratio measured for a series of Pb solutions with different Pb concentrations. The raw isotope ratios were recalculated using different dead time settings and the optimum dead time was obtained by plotting linear regression lines through the data with a gradient of zero (*i.e.* the dead time was independent of concentration). The dead time for each ion counter on an MC-ICP-MS was recently ascertained by measuring isotopic ratios in U series solutions (IRMM-072) and Ba, Lu and W solutions in static mode, which makes the procedure independent of plasma instability and therefore is an ideal method for MC-ICP-MS instruments.[7,30]

The reason for the non-linear response of ion counters is still not well understood. A non-linear response results in relatively more pulses counted at higher beam intensities,[31,33] perhaps due to a memory effect. At higher beam intensity, sustained elevated SEM yield over 15–20 s suggests that each new pulse might experience interference from a decaying predecessor pulse. In contrast, Zhang *et al.* (2015)[34] observed the opposite phenomenon, low SEM responses at count rates higher than a threshold of ~320 000 cps. Furthermore, Hoffmann *et al.* (2005)[33] observed that the nonlinearity starts at count rates as low as 10 cps, much lower than that of the 10^4 to 10^5 cps threshold reported by Richter *et al.* (2001).[31] Richter *et al.* (2009, 2016)[30,39] reported insignificant non-linearity in the responses of SEMs on the same ion counters (MasCom) used by Zhang *et al.* (2015).[34] These studies highlight the importance of detailed characterization of each ion counter on a new system. In order to avoid the influence of typical ion beam intensity fluctuation, combined SEM–Faraday cup measurements in static mode, where the SEM is used to detect a low-abundance isotope of a certified isotopic reference material and Faraday cups detect the major isotopes, may be more suitable for determining nonlinearity effects than the peak jump method.[30,33,39]

3.2 Challenges in U–Th–Pb geochronology

3.2.1 Common lead correction. Horstwood *et al.* (2003)[2] showed that, for U–Th–Pb geochronology in accessory minerals with low ratios of radiogenic Pb to common Pb (monazite, apatite, and titanite), a robust common-Pb correction is essential. Common Pb may come from (1) contamination on the sample surface, which can be easily removed by pre-ablation (cleaning pulses) or by rejecting the first few seconds of analysis; (2) carrier gases (He and Ar), which can be minimized using an active carbon or gold trap (*e.g.*, ref. 40–43), or accurately corrected for, and (3) the accessory mineral itself, where common lead occurs in grain defects or in the lattice.

Common Pb from the accessory mineral itself can be corrected for by using Tera and Wasserburg (1972)[44] concordia or isochron plots of a suite of co-genetic grains with a large spread in common Pb/radiogenic Pb ratio, which do not require an estimate of the initial Pb isotopic composition, or by applying an appropriate initial Pb isotopic composition to individual analyses.[45–47] The first approach can be employed in U–Th–Pb dating with highly variable proportions of common Pb, such as the U–Th–Pb dating studies by LA-MC-ICP-MS for titanite (*e.g.*, ref. 28, 41, 46 and 48), apatite (*e.g.*, ref. 41 and 49), rutile (*e.g.*, ref. 46 and 50) and zircon (*e.g.* ref. 29 and 46), projecting a regression line through a data point without preliminary common-Pb correction data on a Tera–Wasserburg (1972)[44] concordia diagram, to deduce the precise common Pb component on the $^{207}Pb/^{206}Pb$ axis. The $^{238}U/^{206}Pb$ age can then be calculated as the regression lower intercept $^{206}Pb/^{238}U$ age on the concordia (Ludwig *et al.*, 1998).[51]

The alternative approach usually includes three different methods (*i.e.*, ^{204}Pb-, ^{207}Pb- and ^{208}Pb-correction) detailed by Williams (1998)[52], involving estimates of initial Pb composition, which can be obtained by analyzing a low-U co-genetic phase (*e.g.*, K-feldspar or plagioclase) with negligible radiogenic Pb, or from Pb evolution models (*e.g.*, ref. 53). The latter is the only option for U–Th–Pb dating of detrital accessory minerals containing common Pb.[46]

The simultaneous collection of flat-topped peaks during LA-MC-ICP-MS analysis makes it possible to accurately measure

^{204}Pb abundance and correct for the isobaric interference from ^{204}Hg on the basis of the natural ^{202}Hg (or ^{201}Hg)/^{204}Hg ratio. Any additional ^{204}Pb measured during the ablation is assumed to have been derived from the sample (*i.e.*, common-Pb) and is used to correct the ^{206}Pb, ^{207}Pb and ^{208}Pb peaks according to Stacey and Kramers' (1975)[53] common lead model values for ^{206}Pb/^{204}Pb, ^{207}Pb/^{204}Pb and ^{208}Pb/^{204}Pb, given an appropriate estimate of the mineral age without the assumption of concordance. For most zircons, variation in background corrected ^{204}Pb counts is high and the mean abundance is so low that the common Pb correction becomes insignificant (*e.g.*, ref. 5 and 54). ^{204}Pb-correction is theoretically the most precise and accurate way to perform common Pb correction (*e.g.*, ref. 2, 43, 55 and 56); however, the initial ^{206}Pb/^{238}U age estimated from the raw data considerably overestimates the true age when the common Pb/radiogenic Pb ratio is high. To address this, Thomson *et al.* (2012)[56] applied a five-step iterative process using Stacey and Kramers' (1975)[53] common Pb model to accurately reproduce the age of apatite and achieve ages with a precision of <2% (2 s).

Both the ^{207}Pb- and ^{208}Pb-correction methods of U–Th–Pb analyses make assumptions of ideal concordance of ^{206}Pb/^{238}U and ^{207}Pb/^{235}U or ^{208}Pb/^{232}Th without the measurement of ^{204}Pb (*e.g.*, ref. 57). The ^{207}Pb-correction method requires the measurement of ^{238}U/^{206}Pb and ^{207}Pb/^{206}Pb ratios and an appropriate estimate for common Pb composition, which is widely used in U–Pb dating by SIMS (*e.g.*, ref. 58). The ^{208}Pb-correction method is less commonly applied, requiring measurement of ^{208}Pb/^{206}Pb and ^{232}Th/^{238}U ratios and an appropriate estimate of common Pb composition. However, for extremely low Th/U ratios (<0.003) in rutile, where almost all of the ^{208}Pb measured is from common Pb, the ^{208}Pb-correction method can be routinely applied as an initial common lead correction.[59]

3.2.2 Downhole fractionation. Laser-induced downhole fractionation means that the measured ratios between different elements vary with depth during laser ablation, a phenomenon related to volatility differences. In the cooling vapor plume produced by laser ablation, the refractory elements (such as U and the rare earth elements, REEs) condense, while highly volatile elements (such as Pb, Bi and Zn) remain in the gas phase longer due to their lower condensation temperatures.[60] Therefore, the signal intensities of refractory elements generally decrease more rapidly than those of volatile elements.[61] Downhole fractionation typically causes an increase in the observed Pb/U ratios with depth, with minor changes in Pb/Th and Pb/Pb ratios.[60,62–65] Elemental fractionation effects vary with parameters such as laser wavelength, spot size, choice of carrier gas, carrier gas flow rate, and laser pulse energy and duration. This fractionation is the major obstacle to obtaining precise and accurate U–Pb ages by LA-ICP-MS and must be corrected for.[60,64,66–70]

Methods to correct downhole fractionation have been developed and can be subdivided according to whether or not standard–sample bracketing (SSB) is employed in modeling downhole fractionation patterns.[65] For a given laser spot diameter and energy density, time-dependent elemental fractionation can be corrected by (1) using a linear model between elemental ratios and hole depth;[60] (2) using a least squares linear fit of the elemental ratio data for each spot analysis, which does not require all analyses to have the same fractionation pattern;[67] or (3) using exponential curves and smoothed cubic splines to more efficiently correct complex fractionation trends.[65]

However, the popular SSB method takes the average ratio of the time interval in the reference material(s) to correct unknowns, and the reference material is used to correct for instrumental mass fractionation and laser-induced elemental fractionation simultaneously, without any requirement to observe or model the fractionation behavior (*e.g.*, ref. 64 and 71). This approach assumes that the features of downhole fractionation in the reference material can be used to model its effects in the unknowns. A similar method was specifically developed for small volume sampling with high spatial resolution, where all ions measured during an ablation are treated together as "total counts".[72,73]

Laser-induced elemental fractionation of Pb from U is observed to be a linear function of the number of laser pulses (crater depth), and is inversely exponentially correlated with spot size.[60] Therefore, longer (deeper) ablations can require even more severe corrections. Experimental results have demonstrated that the LA-MIC-ICP-MS measured ^{206}Pb/^{238}U ratios for the standard reference zircons 91500 (ref. 74) and GJ-1 (ref. 64) are stable in the first 1.3 μm of the ablation (approx. 10 pulses and 130 nm per pulse) and then increase with increasing ablation depth (Fig. 2) (using a G2 laser ablation system at a laser fluence of 4 J cm^{-1}, repetition rate of 4 Hz and beam size of 5 μm).[5] This shows that shallow ablations can reduce the degree of laser-induced downhole fractionation.[5,7]

3.2.3 Matrix effect. If the accuracy and precision of the results obtained using any given analytical technique are dependent on the physical properties or chemical composition

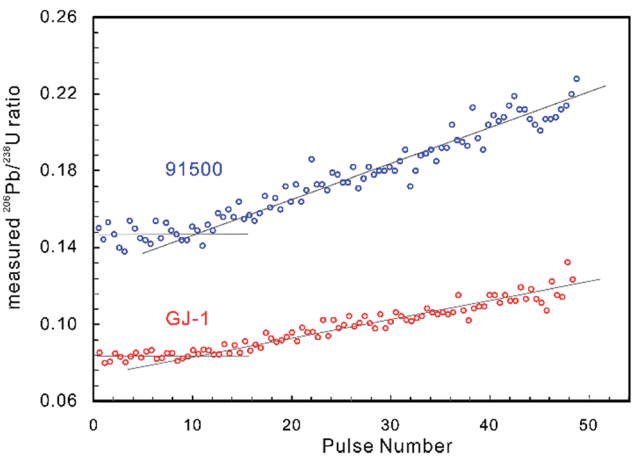

Fig. 2 The measured ^{206}Pb/^{238}U ratios of zircon reference materials 91500 (in blue) and GJ-1 (in red) by LA-MIC-ICP-MS show that the ratio is stable to a depth of about 1.3 μm (approx. 10 pulses and 130 nm per pulse) and then increases as the ablation continues (G2 laser ablation system at a laser fluence of 4 J cm^{-1}, repetition rate of 4 Hz and beam size of 5 μm).

of the sample, that technique suffers from 'matrix effects'. For laser ablation, laser–solid interactions can produce chemically- and size-fractionated sample particles, which leads to differential transport and incomplete ionization of particles in the plasma, resulting in elemental fractionation.[75] These matrix effects are important factors influencing elemental fractionation and, given that the aim of laser ablation is to create an aerosol with a chemical composition identical to that of the sample, pose a serious challenge to accurate and precise elemental and isotopic measurement. For example, Košler *et al.* (2005)[68] demonstrated that 266 nm nanosecond laser ablation (ns-LA) of silicate glass and zircon under identical experimental conditions can produce aerosols with different particle size distributions, morphologies, and phase and chemical compositions, critically impacting the efficiency of transport and ionization.[76]

If the pulse width of the laser is greater than the electron–photon relaxation time of the target, heat is transferred to the sample and elemental fractionation can occur.[77] The short pulse width of femtosecond lasers addresses this issue, theoretically reducing fractionation, especially between volatile and refractory elements of particular interest such as Pb and U.[78–81] Femtosecond laser ablation (fs-LA) offers additional advantages over ns-LA with the production of more uniform and favorably sized particles (about ~0.1–0.2 μm), enhancing transport and ionization efficiency, and enhancing precision, accuracy and detection limits.[76,79,80] This reduction in matrix effects and potential elimination of laser-induced fractionation has obvious implications for LA geochronology.[82] Horn and Blanckenburg (2007)[83] illustrated that elemental fractionation between Pb and U was absent during fs-LA and that no matrix match between the standard and the sample was needed. Kimura *et al.* (2011)[84] indicated that there was no downhole fractionation of $^{206}Pb/^{238}U$ using 200 nm ultra-violet fs-LA.

However, the elemental fractionation effect is not totally eliminated under some fs-LA experimental conditions. Laser-induced downhole fractionation of ^{206}Pb and ^{238}U was detected during zircon dating using a 260 nm NWR fs-LA and attributed to thermal effects by Hattori *et al.* (2017)[7], although the observed fractionation was smaller than that induced during ns-LA. In addition, comparable elemental fractionation effects have been noted using 193 nm nanosecond-LA (ns-LA), 265 nm fs-LA and 795 nm fs-LA,[85,86] and elemental fractionation was observed on $^{66}Zn/^{65}Cu$ and $^{208}Pb/^{238}U$ ratios in the aerosol produced by fs-LA of silicate glass (SRM NIST 610) by Koch *et al.* (2006).[87] Heat diffusion processes can penetrate a zone encompassing several hundreds of nm even using short pulse length fs-LA,[88] and the chemical composition of aerosols produced during the fs-LA of natural and synthetic solids is dependent on particle size and morphology as pronounced element partitioning into different particle size fractions has been observed.[89] Furthermore, these particles vaporize at different positions within the ICP, so non-matrix matched quantification capabilities will be limited.[90] Kimura *et al.* (2011)[84] demonstrated that 200 nm fs-LA yielded absolute $^{206}Pb/^{238}U$ ratios that deviated from the natural ratios in zircon by 1.4% when synthetic glass was utilized as a standard, indicating that performing fs-LA solid analyses using non-matrix matched calibration may restrict accuracy.[91] These studies indicate that fs-LA may offer improvements over ns-LA, but that matrix matching of standards and unknowns is still recommended at this stage.

The SSB method assumes that reference materials and unknowns behave identically during ablation. It is essential to age determination accuracy that the mineral unknown analyses are bracketed by a reference material of the same phase (*e.g.*, using a zircon reference material to normalize zircon unknowns). Using non-matrix matched reference materials can result in a 10–20% age offset from the TIMS age.[56,92] To complicate matters, even in single mineral phases, features such as accumulated radiation damage, trace element composition, crystal colour and crystallographic orientation could affect ablation efficiency and consequently limit accuracy and precision. Therefore, any reduction in matrix differences between unknowns and reference materials will improve age accuracy and precision.[93]

Most matrix effect studies focus on zircon dating (*e.g.*, ref. 93–98) and reveal that the laser ablation rate in zircon is dependent on the optical and mechanical character of the zircon matrices.[99] The optical and physical properties of zircons change with their crystalline state, which is governed by lattice defects caused by both radiation damage and the substitution of certain trace elements within the zircon crystal structure.[100,101] For example, the laser penetration rate correlates positively with increased structural strain and distortion due to ion substitution into the Zr crystallographic site by REEs and Hf, and/or into the Si site by P although this dependence is not very significant.[94,102] Changes in ablation rate could also reflect the degree of structural damage produced by alpha-decay,[93,97–99,102] optical and mechanical properties of different crystallographic planes,[103] crystal orientation and change in crystal color.[99,102] In addition, a slight increase in laser fluence produces a subtle increase in penetration depth (1–2 μm for 200 pulses) and a significant increase in the $^{206}Pb/^{238}U$ ratio (1–2%) measured by LA-ICP-MS. A systematic age bias (relative to ID-TIMS) is strongly correlated with the offset in ablation rates between the 'standard' and the 'unknown' (Fig. 3).[99] However, structural damage produced by alpha-decay plays the most important role in defining the ablation behavior of zircon[102] and the ablation behavior in turn affects the amount of laser-induced U–Th–Pb fractionation, the magnitude and accuracy of the correction required and the subsequent accuracy and precision of ages calculated.[104]

In order to improve matrix effect corrections, several studies have attempted to establish a firm relationship between the degree of radiation damage and parameters that can be used as proxies for the ablation rate and/or penetration depth. For example, the systematic offset in LA-ICP-MS ages relative to the ID-TIMS age is positively correlated with the alpha dose per gram calculated from U and Th concentrations and U–Pb age, and with FWHM values (FWHM = full width at half maximum of the $\nu 3$ (SiO_4) band measured by Raman spectroscopy, which is directly proportional to the amount of radiation damage accumulated in the zircon structure).[97–99,102,104,105] Based on these

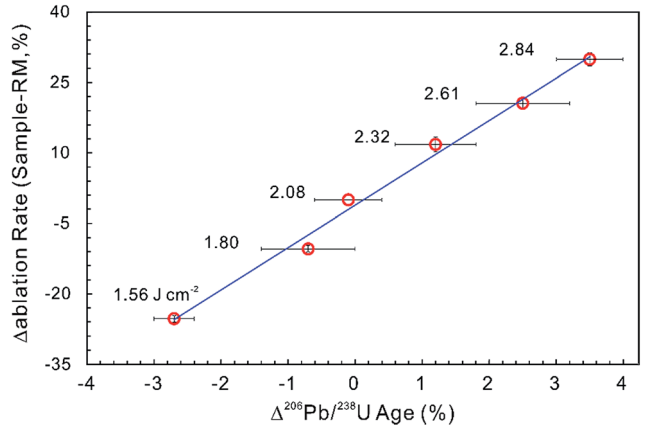

Fig. 3 The influence of ablation rate on corrected LA-ICP-MS $^{206}Pb/^{238}U$ ages. Different energy densities (given in J cm^{-2}) were used to achieve slightly different ablation rates. The ablation rate offset was calculated relative to the ablation rate of the 'standard' zircon at a laser fluence of 2.08 J cm^{-2}. The age offset was calculated for the measured LA-ICP-MS $^{206}Pb/^{238}U$ age relative to the accepted ID-TIMS age. Error bars represent 2SE uncertainty (data from ref. 99).

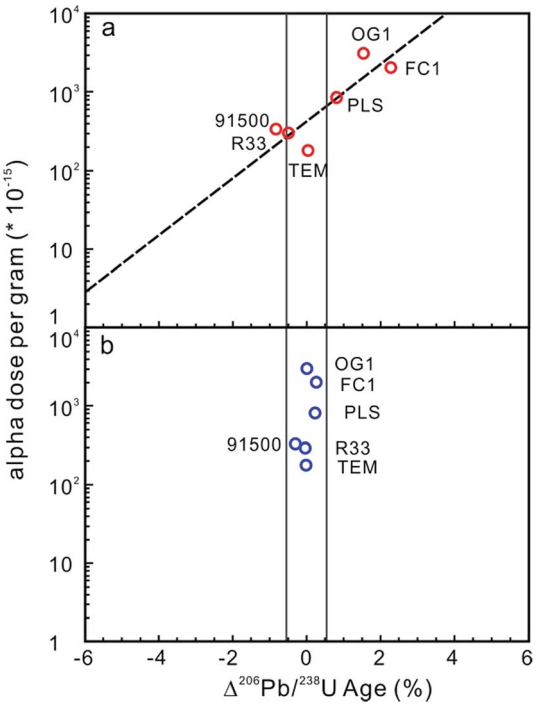

Fig. 4 (a) The effect of alpha dose on the corrected $^{206}Pb/^{238}U$ age for the zircon analyses. The *x*-axis is the percentage offset in the $^{206}Pb/^{238}U$ age measured by LA-ICP-MS and ID-TIMS. The *y*-axis is the corresponding alpha dose calculated from the average U and Th contents and the ID-TIMS age. The field shown is the 2 standard error internal precision for Temora 3 (primary reference standard treated as an unknown), which is 0.51%. The percentage offset in the $^{206}Pb/^{238}U$ age showed obvious correlation with the alpha dose, indicating that differences in the alpha dose between 'standards' and 'unknowns' could result in inaccurate and imprecise $^{206}Pb/^{238}U$ ages. (b) The percentage offsets in the $^{206}Pb/^{238}U$ age for zircon analyses after annealing. The *y*-axis is the same as in Fig. 3a. The *x*-axis is the percentage offset in the $^{206}Pb/^{238}U$ age measured by LA-ICP-MS after annealing relative to that obtained using ID-TIMS. The correlation between the alpha dose and the age offset has been eliminated, indicating that annealing improves accuracy but not internal precision (modified from ref. 97).

studies, it is reasonable to assume that the alpha dose per gram or the FWHM values can be used to predict the laser ablation rate and penetration depth in zircon. However, the calculated alpha dose per gram provides a sensible estimate of the radiation damage only if the zircon structure has experienced no significant annealing of radiation damage since crystallization,[106,107] and obtaining FWHM values for individual crystals is only feasible for a limited number of grains representative of magmatic populations[99,102] and is not practical for detrital studies, for example, where >120 grains per sample are often analyzed to derive statistically significant population distributions (*e.g.*, ref. 105–109).

Potential approaches to reducing the difference in radiation damage between zircon reference materials and unknowns (and thereby reduce differences in laser penetration) include applying thermal annealing to repair crystal-lattice damage[97,102,104] and/or chemical abrasion to remove domains in which Pb loss has occurred.[110,111] Allen and Campbell (2012)[97] demonstrated that the percentage offset between ID-TIMS and LA-ICP-MS $^{206}Pb/^{238}U$ ages showed an obvious correlation with the alpha dose per gram, suggesting that any difference in the alpha dose between 'standards' and 'unknowns' could result in inaccurate and imprecise $^{206}Pb/^{238}U$ ages (Fig. 4a). The correlation between the alpha dose and the age offset was eliminated after thermal annealing, showing that annealing can efficiently repair the crystal-lattice of zircon (Fig. 4b), yielding more accurate, but not necessarily more internally precise, LA-ICP-MS $^{206}Pb/^{238}U$ ages. Solari *et al.* (2015)[112] demonstrated that thermal annealing prior to zircon LA-ICP-MS analyses not only produced more accurate U–Pb ages, but also significantly reduced the scatter of the U–Pb age, trace element content and Hf isotope data. A comparison between thermal annealing of samples at 850 °C for 48 h and 1000 °C for 36 h by Marillo-Sialer *et al.* (2016)[102] indicated that incomplete reconstitution of the crystal structure occurs for partially to highly metamict zircon matrices treated at 850 °C. It follows that pre-analysis annealing of reference and unknown zircons could improve the accuracy of LA-ICP-MS zircon U–Pb dating.

3.3 Ultra-high spatial resolution U–Th–Pb dating

U–Th–Pb geochronology of accessory minerals (*e.g.*, zircon, monazite, apatite, rutile and titanite) has become one of the most powerful techniques for dating a variety of high temperature igneous and metamorphic events, and to constrain provenance.[113,114] The complex zonation in natural crystals with inherited cores and younger rims has tremendous potential for unraveling complicated geological histories. However, analysis of these complex accessory minerals, together with the analysis of tiny mineral grains (*e.g.*, zircon from ultramafic rocks) or subdomains in larger crystals (*e.g.*, in monazite), requires *in situ* dating techniques with high spatial resolution.[5] Modified collector configurations coupling Faraday collectors with ion

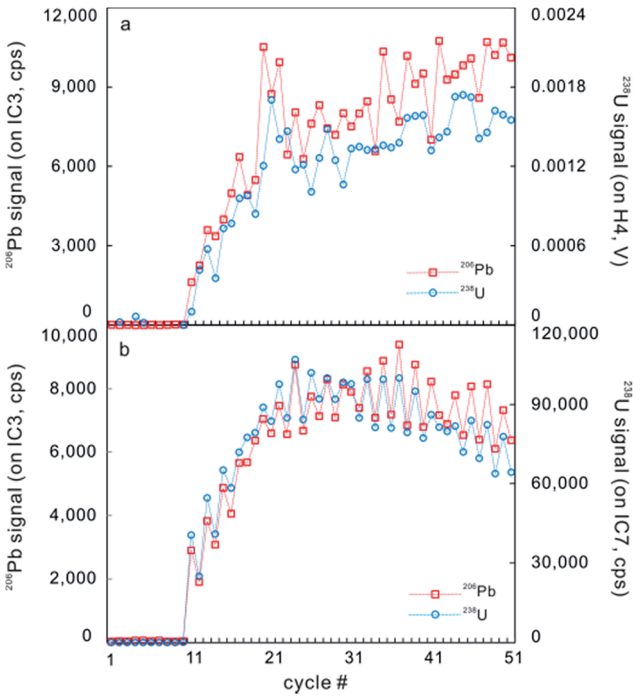

Fig. 5 A typical time-resolved profile on GJ-1 zircon for continuous laser ablation analysis measured on a Neptune Plus. (a) Signals of ^{206}Pb (red) and ^{238}U (blue) were counted on IC3 and Faraday cup H4, respectively. (b) Signals of ^{206}Pb (red) and ^{238}U (blue) were counted on IC3 and IC7, respectively (from ref. 5).

counters are ideally suited to this type of analysis (*e.g.*, ref. 2, 22, 24, 28, 29, 43, 50, 55, 56 and 115–118), enabling signals of <1 mV to be measured with confidence (*e.g.*, ref. 4, 27, 54, 72 and 73).

With Pb and Hg isotopic signals collected on ion counters and U and Th measured on Faraday cups, a spatial resolution of 5–40 μm can be achieved for zircon, monazite, titanite and rutile,[27,50] even in standard petrographic thin sections where textural information is also retained. Simonetti *et al.* (2006)[27] utilized well-characterized external mineral reference materials to correct for mass fractionation and the ^{206}Pb/^{238}U and ^{207}Pb/^{235}U values (obtained from a Nu Plasma MC-ICP-MS equipped with ETP ion counters) were reported at an external reproducibility (2σ) of less than 3%. Furthermore, the aspiration of a Tl solution was used to simultaneously correct for instrumental mass bias in the measured ^{207}Pb/^{206}Pb value, to improve precision (2σ values were between ~0.3 and 1%). Low Pb yields obtained from zircon with intricate isotopic zoning at spatial scales as small as 12–14 μm (diameter) by 4–5 μm (depth, measured with a MicroXAM-100 3D surface profiler) can be determined with a GV Isoprobe MC-ICP-MS equipped with Channeltron detectors and using a total count integration method to calculate U and Pb isotope ratios and ages precisely and accurately within 2%.[72] The technique was successfully applied to provenance studies of detrital zircon in fine-grained mudstones and shales, and to create zircon U–Pb age maps to investigate the detrital and metamorphic history of granulite-facies paragneiss. If water is aspirated during laser ablation analysis, it can double sensitivity and reduce ^{204}Pb signal intensities when the ablated material is carried into the plasma. This method has been applied to age and U/Th ratio mapping of zoned zircon. The results measured with a GV Isoprobe MC-ICP-MS demonstrate that core and rim ages are resolvable (92.6 ± 1.3 Ma and 58.3 ± 1.1 Ma, respectively)[43] and the method, with a smallest pit size of 10 μm diameter and ~3 μm depth measured with an NT9800 optical interferometer, has also been applied to baddeleyite, which is often the smallest datable mineral in samples.[118]

However, after the laser is fired, a signal delay can be observed before the ^{238}U Faraday cup reaches its peak signal intensity relative to the ^{206}Pb ion counter (Fig. 5),[5,73] and this time offset phenomenon can adversely affect data quality. Using a low volume ablation cell, isotope ratios from an individual laser pulse can be calculated by integrating the baseline-subtracted total counts for the entire pulse. This 'total signal integration' method can eliminate the effect of different detector response times and data obtained for reference zircons using a Nu Plasma HR MC-ICP-MS, which indicates that it is possible to consistently measure ^{206}Pb/^{238}U and ^{207}Pb/^{206}Pb ratios with external reproducibilities of 2% and 2.8% (2SD), respectively.[73] Isotopic depth profiles for two grains of zoned

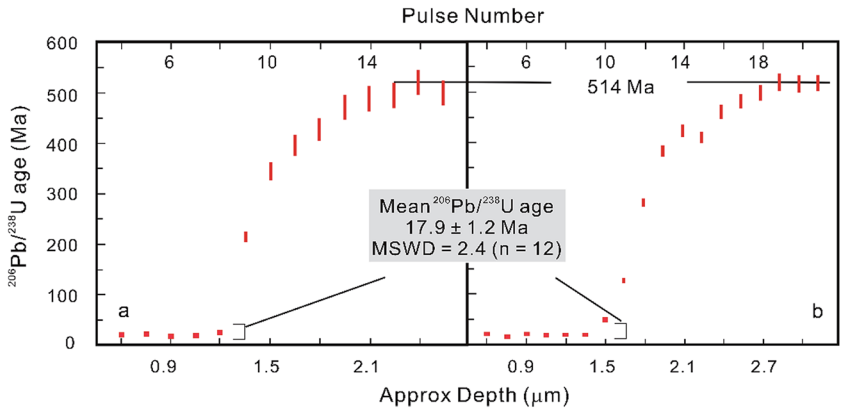

Fig. 6 Consecutive laser pulse analyses of two zoned zircon grains are shown in (a) and (b), indicating that LA-MC-ICP-MS with a MIC system can be applied to isotopic depth profile analysis with a high depth resolution of ~0.1 μm per pulse (modified from ref. 73).

zircon from an augen gneiss sample from the Greater Himalayan Series of north-central Bhutan were generated by analyzing consecutive laser pulses from the same ablation site using a 50 μm spot size and a depth resolution of ~0.1 μm per pulse based on the scanning electron microscope secondary electron images of ablation craters (Fig. 6).[73] Another approach to eliminating the effect of the time offset is to collect all isotopes on ion counters (LA-MIC-ICP-MS).[5,7] For collecting a small signal, the ion counter has an obvious advantage over the Faraday cup (Fig. 1), so this approach can provide higher spatial resolution. LA-MIC-ICP-MS techniques make it possible to date zircon with a ^{238}U signal of less than 0.5 mV at a beam diameter of 5.8–7.4 μm and sampling depth of 1–3 μm (measured by atomic force microscopy) using a laser fluence of 4 J cm^{-2}, with accuracy and precision of less than 1% (2 s) for the weight mean $^{206}Pb/^{238}U$ age (using a Neptune Plus MC-ICP-MS).[5] A 1 s ablation at a fluence of about 1.6 J cm^{-2} (8 laser shots) produced a 25 μm pit with a depth of <1 μm (estimated using a Leica DVM5000 HD digital microscope with 2000× magnification) in zircon standard Plěsovice and yielded a U–Pb concordia age of 339.5 ± 6.7 Ma (ref. 7) (Nu Plasma HR MC-ICP-MS), which is within the uncertainty of the recommended value (337.13 ± 0.37 Ma (ref. 119)). These techniques offer the opportunity to accurately date complex accessory minerals with ultra-high spatial resolution, comparable to that of SIMS techniques.

4. Simultaneous analysis of multiple isotope systems

4.1 Overview

Measurement of U–Th–Pb ages, Sr/Nd/Hf isotopic compositions and trace element contents in minerals using SIMS or LA-SC-ICP-MS, and LA-MC-ICP-MS has historically been conducted sequentially, on different volumetric domains (*e.g.*, ref. 9, 10, 20, 56, 120 and 121). Typical analytical protocols involve (1) age determination *via* SIMS followed by Sr/Nd/Hf isotopic analysis *via* LA-MC-ICP-MS over the shallow SIMS crater (*e.g.*, ref. 122 for Hf isotopes in zircon), (2) measurement of the age and trace elements by LA-SC-ICP-MS using a relatively small pit, followed by LA-MC-ICP-MS Sr/Nd/Hf isotopic analysis using a large crater placed over the top of the earlier age pit, or (3) placing the LA-MC-ICP-MS ablation for Sr/Nd/Hf isotopic analysis near the age pit, but presumably in the same zone as indicated by cathodoluminescence imagery or similar means (*e.g.*, ref. 123–125 for Hf isotopes in zircon; ref. 20 and 126 for Sr and Nd isotopes). For relatively simple samples, these procedures can produce robust results. However, for complexly zoned or detrital/inherited minerals, modeling different geochemical systems using data generated from different analytical volumes could result in erroneous interpretation, particularly as zonation continues at depth and may not be represented by the cathodoluminescence image of the grain surface. In the three analytical approaches outlined above, two very different sample volumes for the U–Th–Pb age and Sr/Nd/Hf isotope composition are measured, which can lead to de-coupling of the age–isotope system and result in inaccurate initial isotope compositions.[15] For example, Harrison *et al.* (2005)[127] dated and determined the Lu–Hf isotopic composition of the >4 billion year old zircons from the Jack Hills metasedimentary belt in Western Australia, a rare and valuable opportunity to elucidate early Earth conditions. Ages were determined using SIMS, on a pit <1 μm deep, while the Hf isotopic composition was determined using LA-MC-ICP-MS with larger spot sizes of 60–80 μm and 1000 times more material analyzed. Extreme heterogeneity in initial εHf (both positive and negative values) was interpreted as reflecting processes of plate tectonics and continental growth on the early Earth. However, later studies by Harrison *et al.* (2008)[128] and Kemp *et al.* (2009)[122] using quasi-simultaneous techniques (see below) revealed a much simpler Lu–Hf evolution for the source materials of the Jack Hills zircons. This emphasizes the importance of simultaneous measurement of multiple isotope systems, an approach which also significantly enhances the analytical throughput and permits analysis of smaller grains that cannot accommodate two analytical spots.[129]

4.2 Quasi-simultaneous analysis

A quasi-simultaneous approach to measure the zircon $^{207}Pb/^{206}Pb$ age and Hf isotope composition was first reported by Woodhead *et al.* (2004),[130] followed by Harrison *et al.* (2008)[128] and Kemp *et al.* (2009).[122] This method involved alternating cycles during a single ablation (*e.g.*, one cycle for Hf analysis and the next cycle for measurement of Pb isotopes) and employed a 193 nm ArF excimer laser-ablation system coupled to a Nu Instruments MC-ICP-MS. Unfortunately, determination of the U–Pb age was not successful, and because $^{207}Pb/^{206}Pb$ dating is generally not suitable for Phanerozoic zircons, the applicability of the method was limited to Precambrian grains. For this reason, an improved method was reported by Xia *et al.* (2011)[131] in which quasi-simultaneous determination Hf isotope composition and U–Pb ages of zircon with a Nu Plasma HR MC-ICP-MS was conducted, allowing the concordance of the measured ages to be assessed, Pb loss to be identified, and physical mixing of cores and rims during analysis to be noted. Nevertheless, this alternative approach does not provide authentic simultaneous measurement of both isotopic systems and the precision of both U–Pb age and Hf isotope ratio also appears to be compromised by the relatively short counting times given the requirement for alternating measurement. Additionally, precious analytical time is lost to magnet settling, depending on the collector configuration (*e.g.*, about 25% and 33% in Kemp *et al.* (2009)[122] and Xia *et al.* (2011)[131], respectively).

4.3 Laser ablation split stream (LASS) methods

Simultaneous *in situ* determination of U–Th–Pb age, trace elements, and Sr/Nd/Hf isotopes from a single laser spot can be accomplished by connecting two independent ICP-MS instruments to a single laser (*e.g.*, ref. 12–15, 17, 132 and 133). The ablated aerosol from the sample cell is split downstream into two separate paths using a "Y" shaped three-way connection pipe. In the most common configuration, one path leads to a MC-ICP-MS for measuring Sr/Nd/Hf isotopes or ages, and the

other passes to a SC-ICP-MS for U–Th–Pb dating and/or trace element analysis. Appropriately, this method is called laser ablation split stream (LASS). Due to the different concentrations of Sr, Nd, Hf, U, Th and Pb in the analyzed minerals, the proportions of ablated aerosol carried into the two sets of ICP-MSs may need to be adjusted in order to obtain both isotopic compositions and U–Pb ages with high precision. Experimental results have shown that there is no significant element or mass fractionation resulting from splitting the ablated product, or from adjusting the proportions of ablated material between MSs.[13,16]

Many mass spectrometry instrument models (*e.g.*, MC-ICP-MSs including Nu Plasma HR, Nu Plasma II, Thermo Neptune and Neptune Plus; and SC-ICP-MSs including Elan 6100DRC, Agilent 7500a and 7700s, Nu AttoM and Element XR) have been applied in LASS analysis and the most common instrument models and applications are summarized in Table 1.

Due to its rapid scanning capability, a single collector quadrupole ICP-MS is a better LASS option than a single collector sector field ICP-MS (*e.g.*, Thermo Fisher Element XR) when a large range of masses are required during a single ablation (*e.g.*, U–Th–Pb + trace elements). However, compared with a single quadrupole ICP-MS, a sector field ICP-MS (Element XR) has about 10× higher sensitivity.[134] The internal and external reproducibility of isotope composition, element concentration and ratio depend primarily on instrument drift, matrix difference between reference materials and samples, signal stability and signal intensity. Typical uncertainties (2 s) are about 1%, 1–2% and 1–3% for $^{206}Pb/^{238}U$ ages measured with a MC-ICP-MS, sector field ICP-MS and single quadrupole ICP-MS, respectively,[12,13,17,132,135] 0.007–0.01% for $^{176}Hf/^{177}Hf$,[12–14,17] 0.01% for $^{143}Nd/^{144}Nd$[16,133] and 0.015% for $^{86}Sr/^{87}Sr$.[16] However, the main limitation of simultaneous measurement of multiple isotope systems is that the signal

Table 1 Summary of minerals and instrument configurations applied in LASS techniques

Isotope system and the mineral	Instrument model/type			Reference
	MC-ICP-MS	SC/MC-ICP-MS	Laser ablation system	
Lu–Hf (MC) and U–Th–Pb–trace elements (SC) for zircon	Nu Plasma HR	Elan 6100DRC	GeoLas Plus	12
Lu–Hf (MC) and U–Th–Pb–trace elements (SC) for zircon	Nu Plasma II	Agilent 7700s	RESOlution LR S155	17
Lu–Hf (MC) and U–Th–Pb–trace elements (SC) for zircon and baddeleyite	Neptune	Agilent 7500a	GeoLas Plus	13
Lu–Hf (MC) and U–Th–Pb (SC) for zircon	Neptune Plus	Element XR	Photon Machines Analyte	14
(1) U–Th–Pb (MC) and trace elements (SC) for zircon and monazite. (2) Lu–Hf (MC) and U–Th–Pb–REE (SC) for zircon	Nu Plasma HR	Nu AttoM	Photon Machines Analyte	132
Lu–Hf (MC) and U–Th–Pb (SC) for zircon	Neptune	Element 2	NewWave 213 nm Nd:YAG	15
Sm–Nd (MC) and U–Th–Pb (SC) for monazite	Neptune	Element XR	GeoLas Pro	133
U–Th–Pb (MC) and trace elements (SC) for monazite	Nu Plasma HR	Nu AttoM/Agilent 7700s	Photon Machines Analyte	135
U–Th–Pb (MC) and trace elements (SC) for titanite and zircon	Nu Plasma HR	Agilent 7700x	Photon Machines Analyte	138
(1) Rb–Sr and Sm–Nd for apatite, perovskite, loparite and eudialyte. (2) Sm–Nd and Lu–Hf for eudialyte and zirconolite	Neptune	Neptune Plus	Photon Machines Analyte	16
U–Th–Pb (MC) and trace elements (SC) for titanite	Nu Plasma HR	Nu AttoM	Photon Machines Analyte	139
Sr isotopes (MC) and elemental ratios (SC) for otoliths	Nu Plasma HR	NexION 350D	NWR193	190
Sm–Nd (MC) and U–Th–Pb–REE (SC) for monazite	Neptune	Element 2	NewWave 213 nm Nd:YAG	149
S and Pb isotopes for pyrite, chalcopyrite, galena and sphalerite	Nu Plasma II	Nu Plasma 1700	RESOlution M50A	140

intensity on the individual ICP-MS instruments decreases, compared to that obtained from separate measurements of Sr, Nd, Hf, and U–Pb isotopes and trace elements. Signal intensity can be improved if the He carrier gas is mixed with a small amount of N_2 (less than 5 mL min^{-1}) before it enters the ICP.[136] When measuring Lu–Hf isotopes on a Neptune instrument, the sensitivity can be improved by a factor of about 1.4 if the MS is equipped with a standard nickel sample cone and a nickel "X" skimmer cone.[137] Careful optimization of the make-up gas flow, the carrier gas flow and composition and the proportions of the split between the two MSs is required to obtain optimum precision in all analyses. In addition, laser ablation parameters (including spot size, fluence and frequency) should be optimized because signal intensity also depends on the volume of the ablated material. In fact, not all minerals are suited to the LASS approach due to the limitations of low concentration and potential interference with the isotopes of interest.[16] However, single shot-LASS can be used for high resolution depth profiling (about 100–150 nm per pulse) with some sacrifice of precision (*e.g.*, determining the U–Pb age and trace element concentrations in zircon and titanite by Viete *et al.* (2015)[138] and Stearns *et al.* (2016)[139], respectively).

Sulphide deposit formation usually involves multiple mineralization stages, which produce complicated mineral assemblages (*e.g.*, zoned minerals and simple mineral grains originating at different stages of deposit formation). Deconvolving this multi-stage genesis is critical to the generation of effective exploration models and for prospectivity assessment and LASS can play an important role. Recently, Yuan *et al.* (2018)[140] reported that a laser coupled to two MC-ICPMSs was used to conduct simultaneous analysis of S and Pb isotopes of sulfide minerals from a single ablation of pyrite, chalcopyrite, galena, and sphalerite, expanding the scope of LASS application to studies of mineral deposits.

The raw data produced from two sets of ICP-MSs can be reduced separately but recently Fisher *et al.* (2017)[141] introduced a multiple-DRS functionality into the Iolite software (Paton *et al.*, 2011)[142] for reduction of datasets collected simultaneously *via* the LASS technique. This approach allows the researcher to synchronize, visualize, and simultaneously reduce concurrently acquired multi-stream analyses and will vastly improve our ability to efficiently process large quantities of data.

5. Minerals utilized for U–Th–Pb dating and LASS

In situ U–Pb dating, trace element analysis and isotopic analysis are used in geoscience to resolve a wide range of research questions, often in combination. The choice of analytical approach depends on the scientific aims, the mineralogy of samples and the availability of appropriate instrumentation, standards and methodologies. The size of the targets, concentration of parent and daughter isotopes, approximate age and desired precision should also be considered when analytical strategies are being assessed.

The common accessory phases zircon and monazite commonly contain high U concentrations and low common lead content. Both have a relatively high U–Pb closure temperature (more than 800 °C for zircon;[143] about 750 °C for monazite[144]) and strong physical and chemical resistance during post-crystallization processes, designating them as priority targets for placing age constraints on high-temperature geological events. Zircon U–Th–Pb–Hf–O isotopic systems and trace element signatures are utilized extensively as zircon is ubiquitous in most rock types.[145,146] Accessible to either ion or laser probe techniques, zircon is an ideal mineral for LASS research where age, trace element composition, and Lu–Hf isotopic signatures can be obtained from a single laser spot (25–60 μm), owing to its low concentration of Lu.[12–15,17,132,147] Monazite has a high Th content (up to 20% (ref. 148)) and can be utilized for Th–Pb dating. Elemental signatures (*i.e.*, REEs) in complex monazite grains are linked to formation age and can inform the crystallization sequence and metamorphic processes (*e.g.*, ref. 25 and 148). Monazite is suited to LASS for Sm–Nd–U–Th–Pb isotope and trace element analysis and the spot size can be reduced if the concentration of the elements of interest is high enough (the beam diameter is usually 10–60 μm depending on the application) (*e.g.*, ref. 132, 133 and 135). Recently, the Sm–Nd and U–Th–Pb isotope systems and trace element signatures in detrital monazite have been applied to a crustal evolution study, comparing the age and tracer isotope signatures in sediments from two large rivers draining the South China block.[149]

Other high U minerals suited to U–Th–Pb dating are apatite, titanite (sphene) and rutile, common accessory minerals in natural samples but with relatively high common lead content. The U–Pb closure temperatures are 450–550 °C for apatite,[150] 650–700 °C for titanite[151] and 640–510 °C for rutile,[152] and thus their U–Pb ages can constrain mid- to high-temperature geological events, such as metamorphism and hydrothermal alteration (*e.g.*, ref. 153–156). In terms of trace elements, apatite is usually characterized by high Sr and Nd contents (up to several thousand ppm) and extremely low Rb/Sr ratios (normally $^{87}Rb/^{86}Sr < 0.0001$).[10,157] Therefore, apatite is suited to Sr and Nd isotopic analysis (*e.g.*, ref. 10, 158 and 159) and U–Pb geochronology by LA-MC-ICP-MS (*e.g.*, ref. 45, 46, 56, 157 and 160) and will no doubt be utilized for LASS Nd–Sr–U–Th–Pb isotope and trace element analysis in future. The crystal structure of titanite can accommodate high levels of trace elements including REEs, F, Nb, Ta, Zr, Hf, U, Th, Sr, Sn and Pb,[161] making it useful for geochemical and isotopic fingerprinting of geological processes.[47,162] *In situ* Sm–Nd isotope analyses of titanite have been conducted using LA-MC-ICP-MS methods (*e.g.*, ref. 163–165). For zoned titanite, high resolution depth profiling with simultaneous measurement of U–Pb isotopes and trace element concentrations using single shot LASS can distinguish between cooling and (re)crystallization ages, and determine the potential for preservation of thermally mediated diffusive loss profiles.[138,139] The incorporation of Zr into rutile during formation is strongly temperature-dependent, so rutile can be potentially used for both geochronology and/or Zr-in-Rutile (ZiR) thermometry.[166] However, the typically low U content in

rutile may limit its applicability to LASS, particularly for small grains.

A serious issue in laser ablation U–Th–Pb dating of apatite, titanite and rutile is the lack of well-characterized matrix-matched reference materials with low common lead. For apatite, several LA-ICP-MS geochronology reference materials with a range of ages are widely available including Durango,[167] McClure Mountain,[168] Kovdor, Otter Lake and Slyudyanka,[45] MAD,[56] SDG,[49] AP1 and AP2 (ref. 169), and NW-1 (ref. 157). Among these materials, NW-1 apatite, extracted from a carbonatite collected from the Prairie Lake alkaline–carbonatite complex in Ontario, Canada, is probably the best characterized over a range of isotopic systems, and has the lowest common lead content (0.75 ppm, with a ^{204}Pb-based f_{206} of 0.5–4.4% (ref. 160)). NW-1 has a ^{206}Pb–^{238}U age of 1168.3 ± 4.5 Ma (ref. 157), ^{143}Nd/^{144}Nd ratio of 0.512104 ± 11 and ^{87}Sr/^{86}Sr ratio of 0.702504 ± 19.[10] Several titanite age reference materials are widely available including Khan,[170] BLR[171] and OLT.[172] However, the recently characterized MKED1 titanite,[162] sampled from the skarn rocks of the Elaine Dorothy Cu–Au–REE prospect at Mount Isa Inlier, Queensland, Australia, contains the lowest levels of common Pb (<0.5 ppm, ^{206}Pb/^{204}Pb > 6000) and is also characterized for ^{143}Nd/^{144}Nd (0.510365 ± 3) and age (^{206}Pb–^{207}Pb age of 1521.02 ± 0.55 Ma). Commonly utilized natural rutile reference materials for LA-ICP-MS geochronology include R10, R19 and Diss,[173] R13 and JIMP-1B,[174] Sugluk-4 and PCA-S207 (ref. 50), and R632.[1] Among these materials, Axelsson *et al.* (2018)[166] reported that R632 has a relatively low common Pb content (<1%; f_{206}% < 1%), a relatively high U content (>300 ppm) and a moderate U–Pb age of 496 ± 3 Ma. Furthermore, the homogeneous and high Zr content of R632 (4294 ± 196 ppm) makes it a suitable reference material for Zr-in-rutile thermometry. These characteristics may facilitate standardization for rutile LASS U–Pb and trace element analysis.

In addition to the minerals outlined above, baddeleyite, allanite, perovskite, eudialyte, xenotime, zirconolite, loparite, columbite–tantalite, bastnaesite, calzirtite, schorlomite, andradite-rich garnet and cassiterite have either been utilized in U–Pb geochronology and/or LASS isotopic analysis, or are potential candidate minerals, although in many cases, matrix matched standards are scarce or not yet available. Example reference materials include Phalaborwa and SK10-2 for baddeleyite,[9,175] EM-1 and LE40010 for allanite,[176,177] AFK for perovskite,[178] LV01 for eudialyte,[179] MG-1 and BS-1 for xenotime,[180] ZrKA for zirconolite (calzirtite),[181] LOP01 for loparite,[182] coltan 139 for columbite,[183] and K-9 for bastnaesite.[10,184,185]

Zr-bearing minerals like eudialyte, zirconolite and calziritite are ideally suited for U–Th–Pb dating and Nd–Hf–(Sr) isotopic analysis by LA-(MC)-ICP-MS. Eudialyte, one of a group of complex Na–Ca zirconosilicate minerals that generally occur in peralkaline agpaitic syenites, is the only mineral investigated to date for which it is possible to simultaneously determine U–Pb ages and Sr, Nd and Hf isotopic compositions.[179] Huang *et al.* (2015)[16] simultaneously measured Nd–Hf isotopes for eudialyte and zirconolite using two MC-ICP-MS instruments (Neptune and Neptune Plus). The calcium- and titanium-bearing zirconosilicates, zirconolite and calzirtite, also have potential for U–Pb age determination together with Hf–Nd, and possibly Sr, isotopic analysis.[181]

Yang *et al.* (2009)[186] reported precise *in situ* U–Pb age, trace element content, and Sr–Nd isotopic analysis of perovskite by LA-(MC)-ICP-MS (Neptune), in order to obtain the age and initial Sr–Nd isotopic compositions of the Menyin kimberlites. The results are significantly different to data obtained on whole rock samples, indicating that the initial Sr–Nd isotopic ratios of whole rocks are likely to record mixed isotopic signatures, due to crustal contamination and/or subsequent alteration. These authors also described *in situ* analysis of loparite, a perovskite group mineral with extremely low Rb/Sr ratios and high rare earth content, by LA-(MC)-ICP-MS for the determination of U–Pb ages and Sr and Nd isotopic composition.[182] Simultaneous measurement of Sr–Nd isotopes for perovskite and loparite can also be performed by LASS.[16]

Additional ore minerals (bastnaesite, xenotime, columbite–tantalite (coltan) and cassiterite) have been studied for U–Th–Pb dating and determination of Sr or Nd or Hf isotopic composition using LA-(MC)-ICP-MS.[10,187] Analysis of an in-house bastnaesite reference material (K-9) first demonstrated that precise and accurate U–Th–Pb ages can be obtained after common Pb correction with a laser or ion probe.[10,184,185] The moderate Sr and extremely high Nd contents in bastnaesites, but generally low Rb–Sr ratios, also potentially allow for the precise determination of *in situ* Sr–Nd isotopic analyses by LA-MC-ICP-MS or LASS. These results will have significant implications for understanding the genesis of endogenous ore deposits and the formation processes related to metallogenic geochronology. Columbite–tantalite (coltan) is characterized by high U and low common Pb contents, making it an ideal mineral for U–Pb isotopic dating of Nb–Ta mineralization. Che *et al.* (2015)[183] used a coltan U–Pb dating method to date the Nanping pegmatite (NP155), an important Nb–Ta deposit in China.

More recently, U–Pb dating of andraditic or Ti-bearing garnet has become attractive, and, combined with trace element data, will potentially provide a significant tracer tool for carbonates, and alkaline or skarn deposits.[188–190] Seman *et al.* (2017)[189] first presented U–Pb geochronology data for grossular–andradite garnet using LA-SC-ICP-MS and developed three potential reference materials for LA-ICP-MS. However, the sample investigated had a low U content (<10 ppm), in addition to significant amounts of common Pb. Deng *et al.* (2017)[188] demonstrated U–Pb age determination by LA-SC-ICP-MS for andradite-rich garnet in alkaline igneous rocks and skarn deposits. The consistency between the garnet and zircon U–Pb ages confirmed the reliability and accuracy of garnet U–Pb geochronology. Yang *et al.* (2018)[190] reported the first U–Pb geochronological investigation of schorlomite garnet from carbonatite and alkaline complexes and demonstrated its applicability for U–Pb age determination using LA-ICP-MS due to its relatively high U and Th abundances and negligible common Pb content. Garnet U–Pb geochronology is considered to be a promising new technique for understanding the genesis of carbonatites, alkaline rocks, and related rare-metal deposits.

Spatially resolved elemental and isotopic signatures of biological materials have been used to trace the seasonal growth of

organisms. For example, Sr isotopes and elemental ratios were simultaneously measured in otoliths of lenok salmon in order to assess habitat use and migration in a river system.[191]

6. Summary and future focus

LA-MC-ICP-MS techniques can now provide unprecedented levels of precision and spatial resolution in U–Th–Pb accessory mineral geochronology. The flexibility of the approach and the universality of its application are compounded by a high analytical throughput, compared to other methods (*e.g.*, SIMS). For small minerals or those with fine scale growth domains, consecutive single-pulse-analyses (~0.1 μm per pulse) and a short ablation time at a low fluence are the choice for ultra-high resolution isotopic mapping and depth profiling. Accuracy and precision of less than 1% for the $^{206}Pb/^{238}U$ age can be achieved.[4,5,7,73]

The recently developed technique for simultaneous measurement of multiple geochemical systems (LASS) provides geoscientists an opportunity to maintain the integrity of coupled isotopic and geochronological systems while maximizing the amount of data that can be obtained from a single analysis. This approach has proven useful in studies of detrital or metamorphic minerals in areas with complex geological systems that require coupled geochronology, isotopic composition and trace element characterization at high spatial resolution and analytical throughput.

However, some challenges remain in the application of these analytical techniques and future efforts should focus on the following aspects: (1) the procedures for ion counter corrections remain relatively complicated and potentially hinder the broader application of the technique. (2) Matrix effects that limit the accuracy of U–Th–Pb ages can be reduced using fs-LA but can be eliminated if perfectly matrix-matched reference materials are utilized. However, characterization of such reference materials is a challenging and time-consuming process and a simple, broadly applicable correction method would be ideal. Most studies of matrix effects have focused on zircon and perhaps more studies on other minerals are needed. (3) Common lead contamination and interference (Hg) from the plasma gas and carrier gas make it difficult to accurately measure ^{204}Pb and correct for common lead, although this can be partially solved by installing a gold or carbon trap on the gas line or using collision cell gases to remove interference. (4) Normalizing to an accessory mineral reference material without common lead is a popular practice for the correction of mass fractionation. However, apart from the common zircon and monazite reference materials, a reliable reference material without common lead is difficult to find for other accessory minerals. (5) In the application of the LASS technique, the signal intensities measured decrease as the ablated aerosol is divided into two streams for analysis with the instruments. The signal intensities required for reliable measurement of different isotopic systems vary, particularly considering the desired uncertainties in different isotopic ratios (*e.g.*, usually <3% for the $^{206}Pb/^{238}U$ ratio and about 0.01% for the $^{176}Hf/^{177}Hf$ ratio). Therefore, those minerals containing lower concentration of target elements (*e.g.*, Lu–Hf, Rb–Sr and Sm–Nd) are currently not candidates for LASS. Enhancing the sensitivity of MC-ICP-MS, for example, by using a modified cone system and a small volume sample cell, adding N_2 before the aerosol enters the ICP and enhancing the Faraday detection system with amplifiers equipped with 10^{12} or 10^{13} ohm resistors, will improve the flexibility of simultaneous measurement techniques.

Conflicts of interest

There are no conflicts to declare.

Acknowledgements

The authors are grateful for the invitation from the editorial board of JAAS to write this review. Two referees are thanked for their constructive comments, which helped to improve the manuscript significantly. This work was supported by the National Natural Science Foundation of China (No. 41473012 and 41525012).

References

1 J. Walder, I. Platzne and P. A. Freedman, *J. Anal. At. Spectrom.*, 1993, **8**, 19–23.
2 M. S. A. Horstwood, G. L. Foster, R. R. Parrish, S. R. Noble and G. M. Nowell, *J. Anal. At. Spectrom.*, 2003, **18**, 837–846.
3 M. S. A. Horstwood, J. Košler, G. Gehrels, S. E. Jackson, N. M. McLean, C. Paton, N. J. Pearson, K. Sircombe, P. Sylvesterk, P. Vermeesch, J. F. Bowring, D. J. Condon and B. Schoene, *Geostand. Geoanal. Res.*, 2016, **40**, 311–332.
4 J. M. Cottle, A. R. C. Kylander-Clark and J. C. Vrijmoe, *Chem. Geol.*, 2012, **332–333**, 136–147.
5 L. W. Xie, J. H. Yang, Q.-Z. Yin, Y. H. Yang, J. B. Liu and C. Huang, *J. Anal. At. Spectrom.*, 2017, **32**, 975–986.
6 R. N. Taylor, T. Warneke, J. A. Milton, I. W. Croudace, P. E. Warwick and R. W. Nesbitt, *J. Anal. At. Spectrom.*, 2003, **18**, 480–484.
7 K. Hattori, S. Sakata, M. Tanaka, Y. Orihashic and T. Hirata, *J. Anal. At. Spectrom.*, 2017, **32**, 88–95.
8 G. L. Foster and D. Vance, *J. Anal. At. Spectrom.*, 2006, **21**, 288–296.
9 F. Y. Wu, Y. H. Yang, L. W. Xie, J. H. Yang and P. Xu, *Chem. Geol.*, 2006, **234**, 105–126.
10 Y. H. Yang, F. Y. Wu, J. H. Yang, D. M. Chew, L. W. Xie, Z. Y. Chu, Y. B. Zhang and C. Huang, *Chem. Geol.*, 2014, **385**, 35–55.
11 T. E. Johnson, C. L. Kirkland, D. R. Viete, S. Fischer, S. M. Reddy, G. S. Lister, N. J. Evans and B. J. McDonald, *Geosci. Front.*, 2017, **8**, 1469–1478.
12 H. L. Yuan, S. Gao, M. N. Dai, C. L. Zong, D. Günther, G. H. Fontaine, X. M. Liu and C. Diwu, *Chem. Geol.*, 2008, **247**, 100–118.
13 L. W. Xie, Y. B. Zhang, H. H. Zhang, J. F. Sun and F. Y. Wu, *Chin. Sci. Bull.*, 2008, **53**, 1565–1573.

14 D. L. Tollstrup, L. W. Xie, J. B. Wimpenny, E. Chin, C. T. Lee and Q. Z. Yin, *Geochem., Geophys., Geosyst.*, 2012, **13**, Q03017.
15 M. Fisher, J. D. Vervoort and S. A. DuFrane, *Geochem., Geophys., Geosyst.*, 2014, **15**, 121–139.
16 C. Huang, Y. H. Yang, J. H. Yang and L. W. Xie, *J. Anal. At. Spectrom.*, 2015, **30**, 994–1000.
17 C. J. Spencer, A. J. Cavosie, T. D. Raub, H. Roloinson, H. Jeon, M. P. Searle, J. A. Miller, B. J. McDonald and N. J. Evans, *Geology*, 2017, **45**, 975–978.
18 J.-I. Kimura, Q. Chang and H. Kawabata, *J. Anal. At. Spectrom.*, 2013, **28**, 1522–1529.
19 J.-I. Kimura, T. Takahashi and Q. Chang, *J. Anal. At. Spectrom.*, 2013, **28**, 945–957.
20 Y. H. Yang, F. Y. Wu, L. W. Xie, J. H. Yang and Y. B. Zhang, *Acta Pet. Sin.*, 2009, **25**, 3431–3441.
21 A. Cocherie and M. Robert, *Chem. Geol.*, 2007, **243**, 90–104.
22 C. Bouman and J. Schwieters, Scientific, Application Note 30021 of Thermo Fischer Scientific, 2004, 1–6.
23 J. M. Koornneef, C. Bouman, J. B. Schwieters and G. R. Davies, *Anal. Chim. Acta*, 2014, **819**, 49–55.
24 B. J. A. Willigers, J. A. Baker, E. J. Krogstad and D. W. Peate, *Geochim. Cosmochim. Acta*, 2002, **66**, 1051–1066.
25 G. Foster, H. D. Gibson, R. Parrish, M. Horstwood, J. Fraser and A. Tindle, *Chem. Geol.*, 2002, **191**, 183–207.
26 J. I. Kimura, Q. Chang, K. Itano, T. Iizuka, B. S. Vaglarova and K. Tanic, *J. Anal. At. Spectrom.*, 2015, **30**, 494–505.
27 A. Simonetti, L. M. Heamana, T. Chacko and N. R. Banerjee, *Int. J. Mass Spectrom.*, 2006, **253**, 87–97.
28 A. Simonetti, L. M. Heaman, R. P. Hartlaub and R. A. Creaser, *J. Anal. At. Spectrom.*, 2005, **20**, 677–686.
29 A. Cocherie, C. M. Fanning, P. Jezequel and M. Robert, *Geochim. Cosmochim. Acta*, 2009, **73**, 1095–1108.
30 S. Richter, S. Konegger-Kappel, S. F. Boulyga, G. Stadelmann, A. Koepf and H. Siegmund, *J. Anal. At. Spectrom.*, 2016, **31**, 1647–1657.
31 S. Richter, S. A. Goldberg, P. B. Mason, A. J. Traina and J. B. Schwieters, *Int. J. Mass Spectrom.*, 2001, **206**, 105–127.
32 S. M. Nelms, C. R. Quétel, T. Prohaska, J. Vogl and P. D. P. Taylor, *J. Anal. At. Spectrom.*, 2001, **16**, 333–338.
33 D. L. Hoffmann, D. A. Richards, T. R. Elliott, P. L. Smart, C. D. Coath and C. J. Hawkesworth, *Int. J. Mass Spectrom.*, 2005, **244**, 97–108.
34 W. Zhang, Z. C. Hu, L. Yang, Y. S. Liu, K. Q. Zong, H. J. Xu, H. H. Chen, S. Gao and L. Xu, *Geostand. Geoanal. Res.*, 2015, **39**, 467–487.
35 A. A. Van Heuzen, T. Hoekstra and B. van Wingerden, *J. Anal. At. Spectrom.*, 1989, **4**, 483–489.
36 G. P. Russ III in *Applications of Inductively Coupled Plasma Mass Spectrometry*, ed. A. R. Date and A. L. Gray, Blackie, Glasgow, 1989, ch. 4.
37 A. Held and P. Taylor, *J. Anal. At. Spectrom.*, 1999, **14**, 1075–1079.
38 J. P. Valles Mota, J. R. Encinar, M. R. Fernández de la Campa, J. I. Garcia Alonso and A. Sanz-Medel, *J. Anal. At. Spectrom.*, 1999, **14**, 1467–1473.
39 S. Richter, A. Alonso, Y. Aregbe, R. Eykens, F. Kehoe, H. Kühn, N. Kivel, A. Verbruggen, R. Wellum and P. D. P. Taylor, *Int. J. Mass Spectrom.*, 2009, **281**, 115–125.
40 T. Hirata, T. Iizuka and Y. Orihashi, *J. Anal. At. Spectrom.*, 2005, **20**, 696–701.
41 C. D. Storey, T. E. Jeffries and M. Smith, *Chem. Geol.*, 2006, **227**, 37–52.
42 A. K. Souders and P. J. Sylvester, *J. Anal. At. Spectrom.*, 2008, **23**, 535–543.
43 G. E. Gehrels, V. A. Valencia and J. Ruiz, *Geochem., Geophys., Geosyst.*, 2008, **9**, 1–13.
44 F. Tera and G. J. Wasserburg, *Earth Planet. Sci. Lett.*, 1972, **14**, 281–304.
45 D. M. Chew, P. J. Sylvester and M. N. Tubrett, *Chem. Geol.*, 2011, **280**, 200–216.
46 D. M. Chew, J. A. Petrus and B. S. Kamber, *Chem. Geol.*, 2014, **363**, 185–199.
47 C. L. Kirkland, J. Hollis, M. Danišík, J. Peterson, N. J. Evans and B. McDonald, *Precambrian Res.*, 2017, **300**, 107–120.
48 N. R. Banerjee, A. Simonetti, H. Furnes, K. Muehlenbachs, H. Staudigel, L. Heaman and M. J. Van Kranendonk, *Geology*, 2007, **35**, 487–490.
49 H. Y. Zhou, J. Z. Geng, Y. R. Cui, H. K. Li and H. M. Li, *Acta Geosci. Sin.*, 2012, **33**, 857–864.
50 L. Bracciali, R. R. Parrish, M. S. A. Horstwood, D. J. Condon and Y. Najman, *Chem. Geol.*, 2013, **347**, 82–101.
51 K. R. Ludwig, *Geochim. Cosmochim. Acta*, 1998, **62**, 665–676.
52 I. S. Williams, U–Th–Pb geochronology by ion microprobe, in *Applications of microanalytical techniques to understanding mineralizing process, Reviews in Economic Geology*, ed. M. A. McKibben, W. C. Shanks III and W. I. Ridley, 1998, vol. 7, pp. 1–35.
53 J. S. Stacey and J. D. Kramers, *Earth Planet. Sci. Lett.*, 1975, **26**, 207–221.
54 C. Lana, F. Farina, A. Gerdes, A. Alkmim, G. Gonçalves and A. C. Jardim, *J. Anal. At. Spectrom.*, 2017, **32**, 2011–2023.
55 A. Cocherie and M. Robert, *Gondwana Res.*, 2008, **14**, 597–608.
56 S. N. Thomson, G. E. Gehrels and J. Ruiz, *Geochem., Geophys., Geosyst.*, 2012, **13**, Q0AA21, DOI: 10.1029/2011GC003928.
57 K. Ludwig, *Isoplot/Ex, rev. 2.49, A Geochronological Toolkit for Microsoft Excel*, Berkeley Geochronology Center, Berkeley, CA, USA, 2001, Special Publication No. 1a.
58 Q. L. Li, X. H. Li, Z. W. Lan, C. L. Guo, Y. N. Yang, Y. Liu and G. Q. Tang, *Contrib. Mineral. Petrol.*, 2013, **166**, 65–80.
59 T. Zack, D. Stockli, G. Luvizotto, M. Barth, E. Belousova, M. Wolfe and R. Hinton, *Contrib. Mineral. Petrol.*, 2011, **162**, 515–530.
60 I. Horn, R. L. Rudnick and W. F. McDonough, *Chem. Geol.*, 2000, **164**, 281–301.
61 H. P. Longerich, D. Günther and S. E. Jackson, *Fresenius' J. Anal. Chem.*, 1996, **355**, 538–542.
62 J. Košler and P. J. Sylvester, *Rev. Mineral. Geochem.*, 2003, **53**, 243–275.
63 M. Tiepolo, *Chem. Geol.*, 2003, **199**, 159–177.

64 S. E. Jackson, N. J. Pearson, W. L. Griffin and E. A. Belousova, *Chem. Geol.*, 2004, **211**, 47–69.
65 C. Paton, J. D. Woodhead, J. C. Hellstrom, J. M. Hergt, A. Greig and R. Maas, *Geochem., Geophys., Geosyst.*, 2010, **11**, Q0AA06, DOI: 10.1029/2009GC002618.
66 S. M. Eggins, L. P. J. Kinsley and J. M. G. Shelley, *Appl. Surf. Sci.*, 1998, **127–129**, 278–286.
67 J. Košler, H. Fonneland, P. Sylvester, M. Tubrett and R. B. Pedersen, *Chem. Geol.*, 2002, **182**, 605–618.
68 J. Košler, M. Wiedenbeck, R. Wirth, J. Hovorka, P. Sylvester and J. Míková, *J. Anal. At. Spectrom.*, 2005, **20**, 402–409.
69 R. Hergenröder, *J. Anal. At. Spectrom.*, 2006, **21**, 505–516.
70 I. Kroslakova and D. Günther, *J. Anal. At. Spectrom.*, 2007, **22**, 51–62.
71 H. L. Yuan, S. Gao, X. M. Liu, H. M. Li, D. Günther and F. Y. Wu, *Geostand. Geoanal. Res.*, 2004, **28**, 353–370.
72 S. Johnston, G. Gehrels, V. Valencia and J. Ruiz, *Chem. Geol.*, 2009, **259**, 218–229.
73 J. M. Cottle, M. S. A. Horstwood and R. R. Parrish, *J. Anal. At. Spectrom.*, 2009, **24**, 1355–1363.
74 M. Wiedenbeck, P. Alle, F. Corfu, W. L. Griffin, M. Meier, F. Oberli, A. Von Quadt, J. C. Roddick and W. Spiegel, *Geostand. Newsl.*, 1995, **19**, 1–23.
75 S. Zhang, M. He, Z. Yin, E. Zhu, W. Hang and B. Huang, *J. Anal. At. Spectrom.*, 2016, **31**, 358–382.
76 J. Pisonero and D. Günther, *Mass Spectrom. Rev.*, 2008, **27**, 609–623.
77 C. Schäfer, H. M. Urbassek and L. V. Zhigilei, *Phys. Rev. B: Condens. Matter Mater. Phys.*, 2002, **66**, 2–70.
78 M. E. Shaheen, J. E. Gagnon and B. J. Fryer, *Spectrochim. Acta, Part B*, 2015, **107**, 97–109.
79 F. Poitrasson, X. Mao, S. S. Mao, R. Freydier and R. E. Russo, *Anal. Chem.*, 2003, **75**, 6184–6190.
80 F. Poitrasson and F. X. d'Abzac, *J. Anal. At. Spectrom.*, 2017, **32**, 1075–1091.
81 K. P. Jochum, B. Stoll, U. Weis, D. E. Jacob, R. Mertz-Kraus and M. O. Andreae, *Geostand. Geoanal. Res.*, 2014, **38**, 265–292.
82 Z. Li, Z. C. Hu, Y. S. Liu, S. Gao, M. Li, K. Q. Zong, H. H. Chen and S. H. Hu, *Chem. Geol.*, 2015, **400**, 11–23.
83 I. Horn and F. von Blanckenburg, *Spectrochim. Acta, Part B*, 2007, **62**, 410–422.
84 J. I. Kimura, Q. Chang and K. Tani, *Geochem. J.*, 2011, **45**, 283–296.
85 M. Ohata, D. Tabersky, R. Glaus, J. Koch, B. Hattendorf and D. Günther, *J. Anal. At. Spectrom.*, 2014, **29**, 1345–1353.
86 M. Ohata, N. Nonose, L. Dorta and D. Günther, *Anal. Sci.*, 2015, **31**, 1309–1315.
87 J. Koch, M. Walle, J. Pisonero and D. Günther, *J. Anal. At. Spectrom.*, 2006, **21**, 932–940.
88 R. Le Harzic, N. Huot, E. Audouard, C. Jonin, P. Laporte, S. Valette, A. Fraczkiewicz and R. Fortunier, *Appl. Phys. Lett.*, 2002, **80**, 3886–3888.
89 F. X. d'Abzac, A. M. Seydoux-Guillaume, J. Chmeleff, L. Datas and F. Poitrasson, *J. Anal. At. Spectrom.*, 2012, **27**, 108–119.
90 R. Glaus, R. Kaegi, F. Krumeich and D. Günther, *Spectrochim. Acta, Part B*, 2010, **65**, 812–822.
91 D. Günther and B. Hattendorf, *Trends Anal. Chem.*, 2005, **24**, 255–265.
92 J. F. Sun, J. H. Yang, F. Y. Wu, L. W. Xie, Y. H. Yang, Z. C. Liu and X. H. Li, *Chin. Sci. Bull.*, 2012, **57**, 2506–2516.
93 U. Klötzli, E. Klötzli, Z. Günes and J. Košler, *Geostand. Geoanal. Res.*, 2009, **33**, 5–15.
94 L. Black, S. Kamo, C. Allen, D. Davis, J. Aleinikoff, J. Valley, R. Mundil, I. Campbell, R. Korsch, I. Williams and C. Foudoulis, *Chem. Geol.*, 2004, **205**, 115–140.
95 J. Mikova, J. Košler, H. Longerich, M. Wiedenbeck and J. Hanchar, *J. Anal. At. Spectrom.*, 2009, **24**, 1244–1252.
96 E. Kooijman, J. Berndt and K. Mezger, *Eur. J. Mineral.*, 2012, **24**, 5–21.
97 C. Allen and I. Campbell, *Chem. Geol.*, 2012, **332–333**, 157–165.
98 A. Steely, J. Hourigan and E. Juel, *Chem. Geol.*, 2014, **372**, 92–108.
99 E. Marillo-Sialer, J. Woodhead, J. Hergt, A. Greig, M. Guillong, A. Gleadow, N. Evans and C. Paton, *J. Anal. At. Spectrom.*, 2014, **29**, 981–989.
100 R. Ewing, *Rev. Mineral. Geochem.*, 2003, **53**, 387–425.
101 M. Klinger, U. Kempe, A. Pöpl, R. Böttcher and M. Trinkler, *Eur. J. Mineral.*, 2012, **24**, 1005–1016.
102 E. Marillo-Sialer, J. Woodhead, J. M. Hanchar, S. M. Reddy, A. Greig, J. Hergt and B. Kohna, *Chem. Geol.*, 2016, **438**, 11–24.
103 R. Finch and J. Hanchar, in *Structure and chemistry of zircon and zircon-group minerals*, ed. J. M. Hanchar and P. Hoskin, Zircon. Mineralogical Society of America, Washington, DC, 2003, pp. 1–21.
104 J. Thompson, S. Meffre and L. Danyushevsky, *J. Anal. At. Spectrom.*, 2018, **33**, 221–230.
105 L. Nasdala, G. Irmer and D. Wolf, *Eur. J. Mineral.*, 1995, **7**, 471–478.
106 L. Nasdala, P. W. Reiners, J. I. Garver, A. K. Kennedy, R. A. Stern, E. Balan and R. Wirth, *Am. Mineral.*, 2004, **89**, 219–231.
107 P. Vermeesch, *Earth Planet. Sci. Lett.*, 2004, **224**, 441–451.
108 M. Barham, S. Reynolds, C. L. Kirkland, M. J. O'Leary, N. J. Evans, H. Allen, P. W. Haines, R. M. Hocking and B. J. McDonald, *Gondwana Res.*, 2018, **58**, 122–140.
109 V. Markwitz, C. L. Kirkland, K. H. Wyrwoll, L. Hancock, N. J. Evans and Y. Lu, *Tectonics*, 2017, **36**, 2477–2496.
110 A. von Quadt, D. Gallhofer, M. Guillong, I. Peytcheva, M. Waelle and S. Sakata, *J. Anal. At. Spectrom.*, 2014, **29**, 1618–1629.
111 Q. Crowley, R. Key and S. Noble, *Gondwana Res.*, 2015, **27**, 1381–1391.
112 L. A. Solari, C. Ortega-Obregón and J. P. Bernal, *Chem. Geol.*, 2015, **414**, 109–123.
113 A. K. Schmitt, K. R. Chamberlain, S. M. Swapp and T. M. Harrison, *Chem. Geol.*, 2010, **269**, 386–395.
114 V. A. Valencia, J. Ruiz, F. Barra, G. Geherls, M. Ducea, S. R. Titley and L. Ochoa-Landin, *Miner. Deposita*, 2005, **40**, 175–191.

115 J. K. Vry and J. A. Baker, *Geochim. Cosmochim. Acta*, 2006, **70**, 1807–1820.
116 B. Bühn, M. M. Pimentel, M. Matteini and E. Dantas, *An. Acad. Bras. Cienc.*, 2009, **81**, 99–114.
117 L. M. Florisbal, V. A. Janasi, M. F. Bitencourt and L. M. Heaman, *Precambrian Res.*, 2012, **216–219**, 132–151.
118 M. Ibanez-Mejia, G. E. Gehrels, J. Ruiz, J. D. Vervoort, M. P. Eddy and C. Li, *Chem. Geol.*, 2014, **384**, 149–167.
119 J. Sláma, J. Košler, D. Condon, J. Crowley, A. Gerdes, J. Hanchar, M. Horstwood, G. Morris, L. Nasdala, N. Norberg, U. Schaltegger, B. Schoene, M. Tubrett and M. J. Whitehouse, *Chem. Geol.*, 2008, **249**, 1–35.
120 X. H. Li, X. Liang, M. Sun, Y. Liu and X. Tu, *Eur. J. Mineral.*, 2000, **12**, 1015–1024.
121 W. C. McClelland, J. A. Gilotti, F. K. Mazdab and J. L. Wooden, *Eur. J. Mineral.*, 2009, **21**, 1135–1148.
122 A. I. S. Kemp, G. L. Foster, A. Scherstén, M. J. Whitehouse, J. Darling and C. Storey, *Chem. Geol.*, 2009, **261**, 244–260.
123 Y. B. Wu, Y. F. Zheng, Z. F. Zhao, B. Gong, X. Liu and F. Y. Wu, *Geochim. Cosmochim. Acta*, 2006, **70**, 3743–3761.
124 W. L. Griffin, N. J. Pearson, E. Belousova, S. E. Jackson, E. van Achterbergh, S. Y. O'Reilly and S. R. Shee, *Geochim. Cosmochim. Acta*, 2000, **64**, 133–147.
125 T. Iizuka, T. Komiya, S. P. Johnson, Y. Kon, S. Maruyama and T. Hirata, *Chem. Geol.*, 2009, **259**, 230–239.
126 T. Iizuka, O. Nebel and M. T. Mcculloch, *Earth Planet. Sci. Lett.*, 2011, **308**, 350–358.
127 T. M. Harrison, J. Blichert-Toft, W. Muller, F. Albarède, P. Holden and S. J. Mojzsis, *Science*, 2005, **310**, 1947.
128 T. M. Harrison, A. K. Schmitt, M. T. McCulloch and O. M. Lovera, *Earth Planet. Sci. Lett.*, 2008, **268**, 476–486.
129 W. Q. Ji, F. Y. Wu, S. L. Chung, J. X. Li and C. Z. Liu, *Chem. Geol.*, 2009, **262**, 229–245.
130 J. D. Woodhead, J. M. Hergt, M. Shelley, S. Eggins and R. Kemp, *Chem. Geol.*, 2004, **209**, 121–135.
131 X. P. Xia, M. Sun, H. Y. Geng, Y. L. Sun, Y. J. Wang and G. C. Zhao, *J. Anal. At. Spectrom.*, 2011, **26**, 1868–1871.
132 A. R. C. Kylander-Clark, B. R. Hacker and J. M. Cottle, *Chem. Geol.*, 2013, **345**, 99–112.
133 D. J. Goudie, C. M. Fisher, J. M. Hanchar, J. L. Crowley and J. C. Ayers, *Geochem., Geophys., Geosyst.*, 2014, **15**, 2575–2600.
134 M. Wälle and C. A. Heinrich, *J. Anal. At. Spectrom.*, 2014, **29**, 1052–1057.
135 B. R. Hacker, A. R. C. Kylander-Clark, R. Holder, T. B. Andersen, E. M. Peterman, E. O. Walsh and J. K. Munnikhuis, *Chem. Geol.*, 2015, **409**, 28–41.
136 M. Shaheen and B. J. Fryer, *J. Anal. At. Spectrom.*, 2010, **25**, 1006–1013.
137 Z. Hu, Y. Liu, S. Gao, S. Xiao, L. Zhao, D. Günther, M. Li, W. Zhang and K. Zong, *Spectrochim. Acta, Part B*, 2012, **78**, 50–57.
138 D. R. Viete, A. R. C. Kylander-Clark and B. R. Hacker, *Chem. Geol.*, 2015, **415**, 70–86.
139 M. A. Stearns, J. M. Cottle, B. R. Hacker and A. R. C. Kylander-Clark, *Chem. Geol.*, 2016, **422**, 13–24.
140 H. L. Yuan, X. Liu, L. Chen, Z. Bao, K. Y. Chen, C. L. Zong, X. C. Li and J. W. Qiu, *J. Asian Earth Sci.*, 2018, **154**, 386–396.
141 C. M. Fisher, C. Paton, D. G. Pearson, C. Sarkar, Y. Luo, D. B. Tersmette and T. Chacko, *Geochem., Geophys., Geosyst.*, 2017, **18**, 4604–4622.
142 C. Paton, J. Hellstrom, B. Paul, J. Woodhead and J. Hergt, *J. Anal. At. Spectrom.*, 2011, **26**, 2508–2518.
143 D. J. Cherniak and E. B. Watson, *Chem. Geol.*, 2001, **172**, 5–24.
144 H. A. Smith and B. J. Giletti, *Geochim. Cosmochim. Acta*, 1997, **61**, 1047–1055.
145 Y. F. Zheng, Z. F. Zhao, Y. B. Wu, S. B. Zhang, X. M. Liu and F. Y. Wu, *Chem. Geol.*, 2006, **231**, 135–158.
146 J. H. Yang, F. Y. Wu, J. A. Shao, S. A. Wilde, L. W. Xie and X. M. Liu, *Earth Planet. Sci. Lett.*, 2006, **246**, 336–352.
147 R. X. Chen, Y. F. Zheng and L. W. Xie, *Lithos*, 2010, **114**, 132–154.
148 M. J. Kohn and M. A. Malloy, *Geochim. Cosmochim. Acta*, 2004, **68**, 101–113.
149 X. C. Liu, Y. B. Wu, C. M. Fisher, J. M. Hanchar, L. Beranek, S. Gao and H. Wang, *Geology*, 2017, **45**, 103–106.
150 D. J. Cherniak, W. A. Lanford and F. J. Ryerson, *Geochim. Cosmochim. Acta*, 1991, **55**, 1663–1673.
151 D. J. Scott and M. R. St-Onge, *Geology*, 1995, **23**, 1123–1126.
152 E. Kooijman, K. Mezger and J. Berndt, *Earth Planet. Sci. Lett.*, 2010, **293**, 321–330.
153 B. R. Frost, K. R. Chamberlain and J. C. Schumacher, *Chem. Geol.*, 2000, **172**, 131–148.
154 H. Timmermann, V. Štědrá, A. Gerdes, S. R. Noble, R. R. Parrish and W. Dörr, *J. Petrol.*, 2004, **45**, 1311–1338.
155 B. Schoene and S. A. Bowring, *Geochim. Cosmochim. Acta*, 2007, **71**, 165–185.
156 T. A. Ewing, J. Hermann and D. Rubatto, *Contrib. Mineral. Petrol.*, 2013, **165**, 757–779.
157 F. Y. Wu, R. H. Mitchell, Q. L. Li, C. Zhang and Y. H. Yang, *Geol. Mag.*, 2017, **154**, 217–236.
158 M. S. A. Horstwood, J. A. Evans and J. Montgomery, *Geochim. Cosmochim. Acta*, 2008, **72**, 5659–5674.
159 A. L. Henderson, G. L. Foster and Y. Najman, *Earth Planet. Sci. Lett.*, 2010, **297**, 42–49.
160 Q. L. Li, X. H. Li, F. Y. Wu, Q. Z. Yin, H. M. Ye, Y. Liu, G. Q. Tang and C. L. Zhang, *Gondwana Res.*, 2012, **21**, 745–756.
161 M. Tiepolo, R. Oberti and R. Vannucci, *Chem. Geol.*, 2002, **191**, 105–119.
162 C. Spandler, J. Hammerli, P. Sha, H. Hilbert-Wolf, Y. Hu, E. Roberts and M. Schmitz, *Chem. Geol.*, 2016, **425**, 110–126.
163 Y. H. Yang, J. F. Sun, L. W. Xie, H. R. Fan and F. Y. Wu, *Chin. Sci. Bull.*, 2008, **53**, 1062–1070.
164 C. M. Fisher, C. R. M. McFarlane, J. M. Hanchar, M. D. Schmitz, P. J. Sylvester, R. Lam and H. P. Longerich, *Chem. Geol.*, 2011, **284**, 1–20.
165 J. Hammerli, A. I. S. Kemp and C. Spandler, *Earth Planet. Sci. Lett.*, 2014, **392**, 133–142.
166 E. Axelsson, J. Pape, J. Berndt, F. Corfu, K. Mezger and M. M. Raith, *Geostand. Geoanal. Res.*, 2018, **42**, 319–338.

167 F. W. McDowell, W. C. McIntosh and K. A. Farley, *Chem. Geol.*, 2005, **214**, 249–263.
168 B. Schoene and S. A. Bowring, *Contrib. Mineral. Petrol.*, 2006, **151**, 615–630.
169 Q. Zhou, *In situ* U-Pb isotopic dating of accessory minerals in meteorites, Ph. D. Dissertation, University of Chinese Academy of Sciences and Institute of geology and geophysics, Chinese Academy of Sciences(Supervisor of Prof. Fu-Yuan Wu. Chapter 2: 19-22 (in Chinese with English abstract)), 2013.
170 P. D. Kinny, N. J. McNaughton, C. M. Fanning and R. Maas, *ICOG8*, US Geol. Surv. Circ., Berkeley, 1994, vol. 1107, p. 171.
171 J. N. Aleinikoff, R. P. Wintsch, R. P. Tollo, D. M. Unruh, C. M. Fanning and M. D. Schmitz, *Am. J. Sci.*, 2007, **307**, 63–118.
172 A. K. Kennedy, S. L. Kamo, L. Nasdala and N. E. Timms, *Can. Mineral.*, 2010, **48**, 1423–1443.
173 G. L. Luvizotto, T. Zack, H. P. Meyer, T. Ludwig, S. Triebold, A. Kronz, C. Münker, D. F. Stockli, S. Prowatke, S. Klemme, D. E. Jacob and H. von Eynatten, *Chem. Geol.*, 2009, **261**, 346–369.
174 A. K. Schmitt and T. Zack, *Chem. Geol.*, 2012, **332–333**, 65–73.
175 I. Horn, W. F. McDonough and R. L. Rudnick, *Abstract of Ninth Goldschimdt conference*, 1999, p. 7646.
176 D. Rubatto, D. Regis, J. Hermann, K. Boston, M. Engi, M. Beltrando and S. R. McAlpine, *Nat. Geosci.*, 2011, **4**, 338–342.
177 A. J. Smye, N. M. Roberts, D. J. Condon, M. S. Horstwood and R. R. Parrish, *Geochim. Cosmochim. Acta*, 2014, **135**, 1–28.
178 F. Y. Wu, A. A. Arzamastsev, R. H. Mitchell, Q. L. Li, J. Sun, Y. H. Yang and R. C. Wang, *Chem. Geol.*, 2013, **353**, 210–229.
179 F. Y. Wu, Y. H. Yang, M. A. W. Marks, Z. C. Liu, Q. Zhou, W. C. Ge, J. S. Yang, Z. F. Zhao, R. H. Mitchell and G. Markl, *Chem. Geol.*, 2010, **273**, 8–34.
180 I. R. Fletcher, N. J. McNaughton, J. A. Aleinikoff, B. Rasmussen and S. L. Kamo, *Chem. Geol.*, 2004, **209**, 295–314.
181 F. Y. Wu, Y. H. Yang, R. H. Mitchell, F. Bellatreccia, Q. L. Li and Z. F. Zhao, *Chem. Geol.*, 2010, **277**, 178–195.
182 R. H. Mitchell, F. Y. Wu and Y. H. Yang, *Chem. Geol.*, 2011, **280**, 191–199.
183 X. D. Che, F. Y. Wu, R. C. Wang, A. Gerdesc, W. Q. Ji, Z. H. Zhao, J. H. Yang and Z. Y. Zhu, *Ore Geol. Rev.*, 2015, **65**, 979–989.
184 E. B. Sal'nikova, S. Z. Yakovleva, A. V. Nikiforov, A. B. Kotov, V. V. Yarmolyuk, I. V. Anisimova, A. M. Sugorakova and Y. V. Plotkina, *Dokl. Earth Sci.*, 2010, **430**, 134–136.
185 X. X. Ling, Q. L. Li, Y. Liu, Y. H. Yang, Y. Liu, G. Q. Tang and X. H. Li, *J. Anal. At. Spectrom.*, 2016, **31**, 1680–1687.
186 Y. H. Yang, F. Y. Wu, S. A. Wilde, X. M. Liu, Y. B. Zhang, L. W. Xie and J. H. Yang, *Chem. Geol.*, 2009, **264**, 24–42.
187 Z. C. Liu, F. Y. Wu, C. L. Guo, Z. F. Zhao, J. H. Yang and J. F. Sun, *Chin. Sci. Bull.*, 2011, **56**, 2948–2956.
188 X. D. Deng, J. W. Li, T. Luo and H. Q. Wang, *Contrib. Mineral. Petrol.*, 2017, **172**, 71–81.
189 S. Seman, D. F. Stockli and N. M. McLean, *Chem. Geol.*, 2017, **460**, 106–116.
190 Y. H. Yang, F. Y. Wu, J. H. Yang, R. H. Mitchell, Z. F. Zhao, L. W. Xie, C. Huang, Q. Ma, M. Yang and H. Zhao, *J. Anal. At. Spectrom.*, 2018, **33**, 231–239.
191 T. Prohaska, J. Irrgeher and A. Zitek, *J. Anal. At. Spectrom.*, 2016, **31**, 1612–1621.